Electronic Supplementary Material (ESI) for Physical Chemistry Chemical Physics.
This journal is © the Owner Societies 2023

Supporting Information

Ionic and electronic polarization effects in horizontal hybrid perovskite device structures close to equilibrium

Davide Moia,* Mina Jung, Ya-Ru Wang, Joachim Maier

Max Planck Institute for Solid State Research, Heisenbergstr. 1 70569, Stuttgart, Germany

* d.moia@fkf.mpg.de

Contents

1. Interfacial vs Stoichiometric polarization

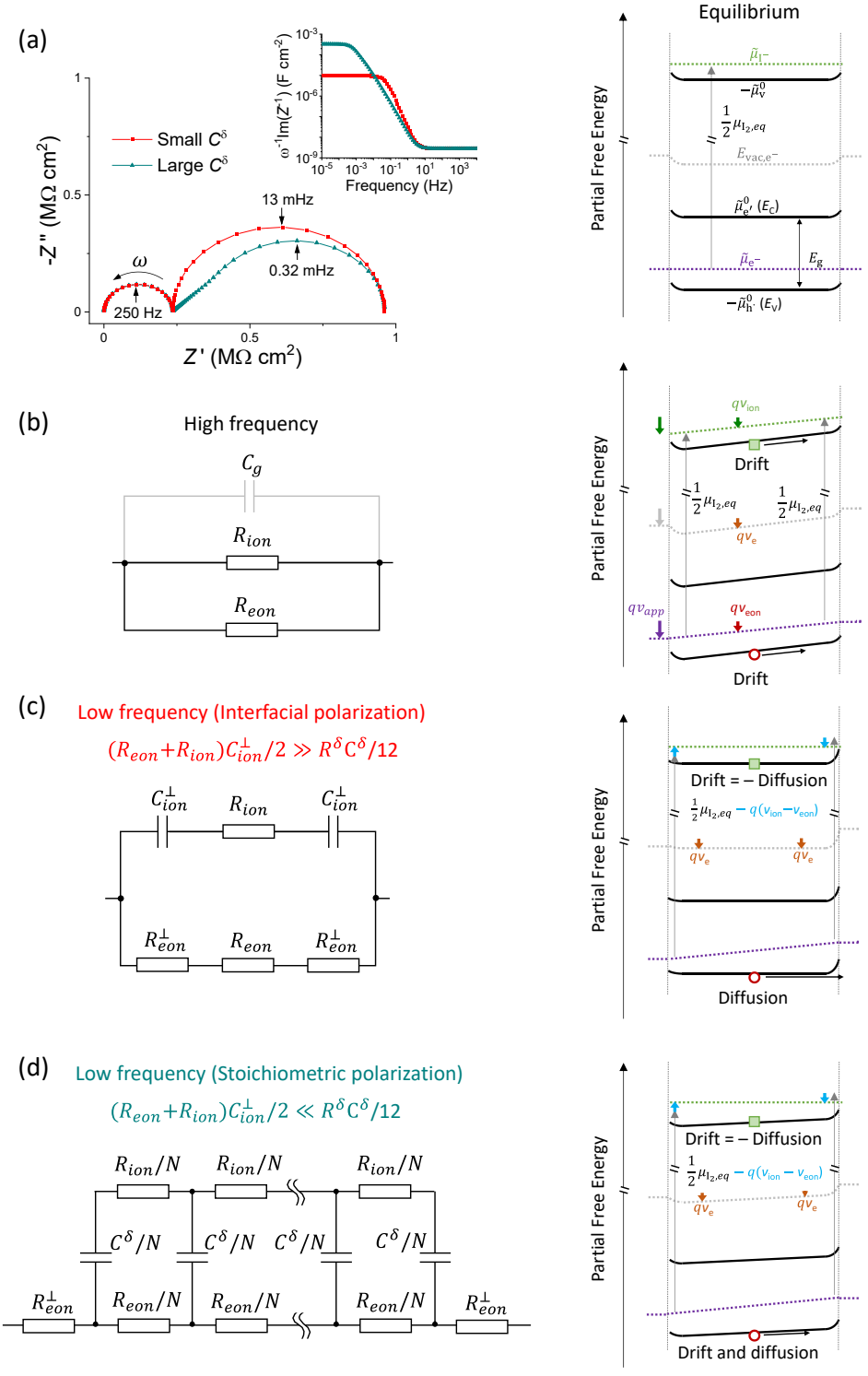

Figure S1. (a) Calculated impedance for the case of large and small chemical capacitance (see also main text). Equivalent circuit model for the (b) high frequency behavior and for the low frequency behavior depending on whether (c) interfacial polarization or (d) stoichiometric polarization dominates the

response. On the right side, the generalized energy diagram situation for each equivalent circuit model is shown (see Ref. 13 in main text). Here, we focus the attention on hole and iodide vacancy transport, relevant to the data in the main text. In the diagram, we show the conduction and valence band edges of MAPI, indicated by $\tilde{\mu}_{\mathrm{e}'}^{0}$ and $-\tilde{\mu}_{\mathrm{h}^{\cdot}}^{0}$, the electrochemical potential of the electrons (Fermi level), $\tilde{\mu}_{\mathrm{e}^{-}}$. In this generalized energy diagram we also show the electrochemical potential of iodide, $\tilde{\mu}_{\mathrm{I}^{-}}$, and standard electrochemical potential of iodide vacancies, $-\tilde{\mu}_{\mathrm{V}}^{0}$. The vacuum level for electrons, $E_{\mathrm{vac,e}^{-}}$, is displayed while we are omitting here the vacuum level of iodide for simplicity. Changes in the potential applied to the device are reflected in the behavior of the changes in electrochemical potentials (v_{p}, v_{ion}) and in changes in $E_{\mathrm{vac,e}^{-}}$, which correspond to changes in the electrostatic potential, v_e. Changes to the local chemical potential of iodine (μ_{I}) from its equilibrium value ($\frac{1}{2}\mu_{\mathrm{I}_2,\mathrm{eq}}$) are shown with light blue arrows and expressed as $q(v_{\mathrm{eon}} - v_{\mathrm{ion}})$. The regime of electronic conduction (drift and/or diffusion) in the different situations is shown.

2. On the evaluation of the total conductivity

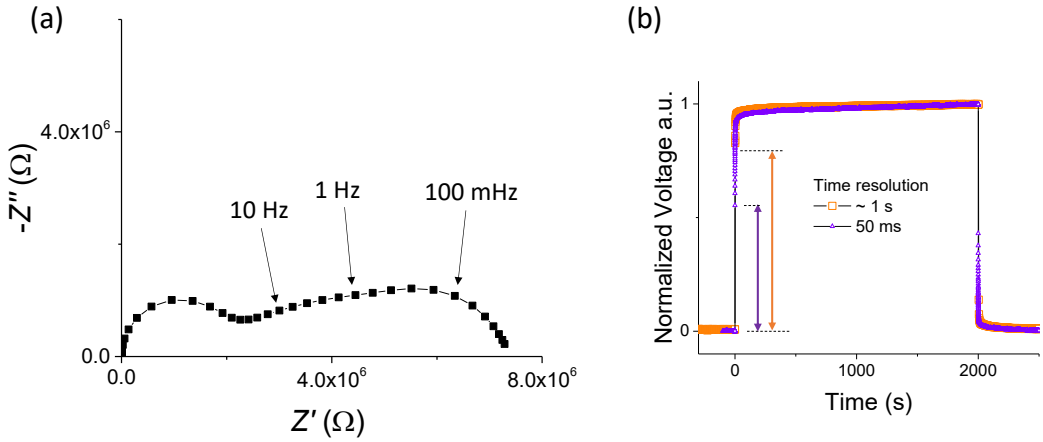

Figure S2. Impedance and DC polarization measurements performed on a MAPI horizontal device under fixed $P(I_2)$ = 4.6 10^{-6} bar. (a) Impedance spectrum highlighting points measured at frequencies corresponding to typical time resolution in time-domain measurements. (b) DC measurements performed with different time resolutions highlighting differences in the extracted value of the "initial voltage jump".

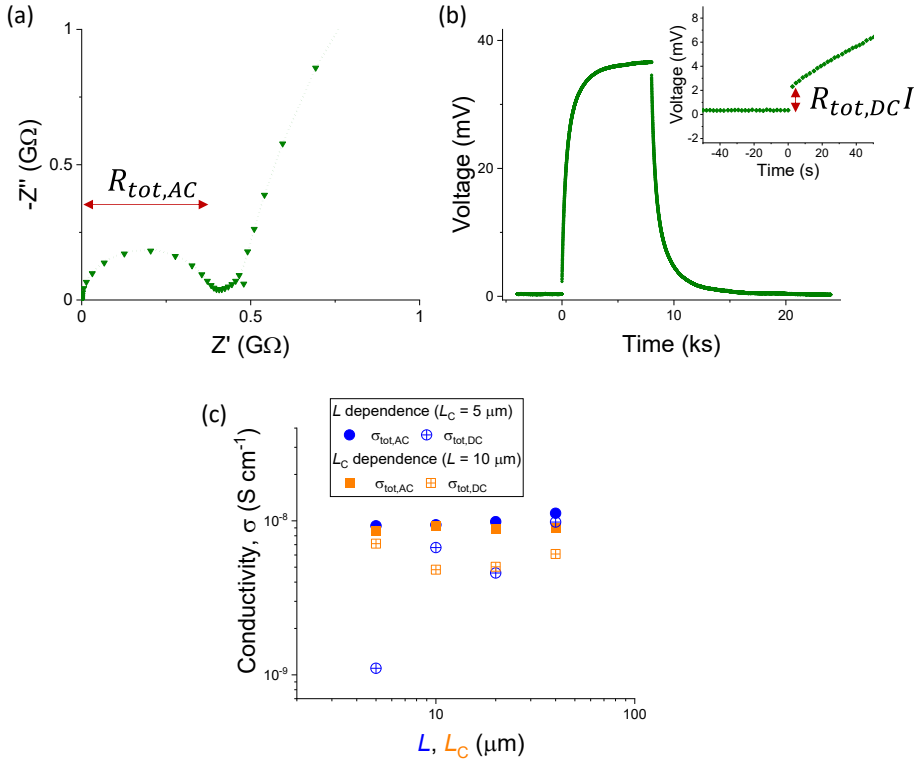

Figure S3. Extraction of the total resistance R_{tot} from either (a) the high frequency feature of the impedance (AC) or (b) the early time scale step in voltage in the DC experiment. (c) Comparison of the resulting conductivities. Values of R_{tot} extracted from the high frequency feature of the impedance spectrum are more consistent across different measurements than the value obtained from the early time scale DC response.

3. Time constant and interfacial resistance

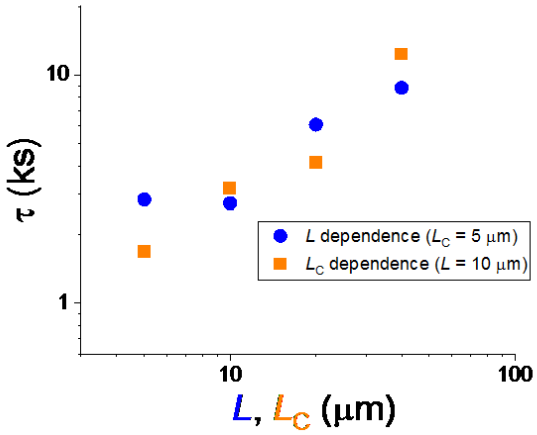

Figure S4. Time constant τ evaluated for the long time scale polarization response obtained from the DC measurements shown in Figure 5 in the main text. Given the dependence of τ on the geometric parameters of the device, its value is associated with interfacial polarization rather than stoichiometric polarization. It follows that it is not possible to extract a chemical diffusivity from the time constant measured in the experiment (see discussion in the main text).

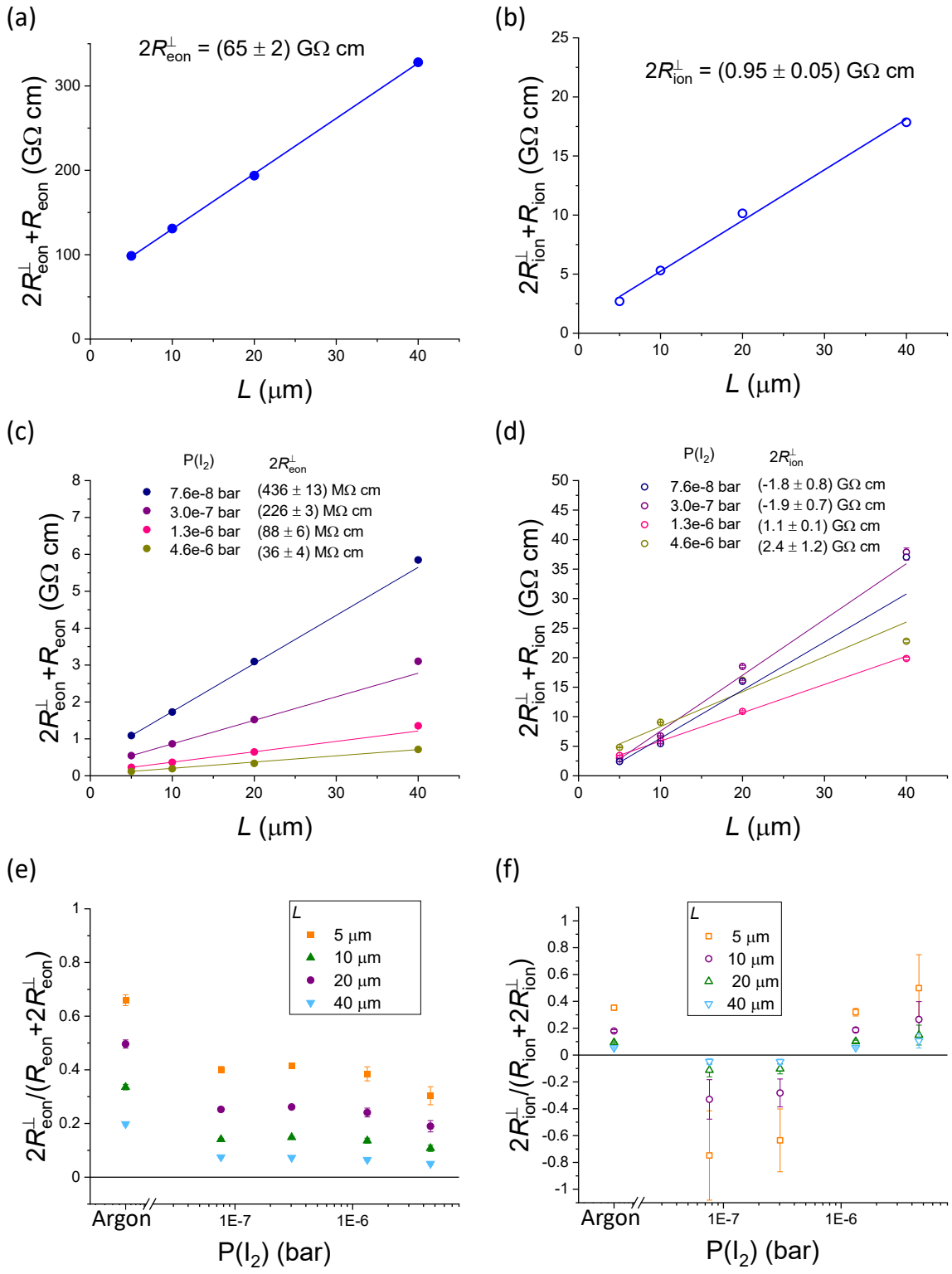

Figure S5. (a, c) Electronic and (b, d) ionic resistance plotted as function of the gap width between the gold electrodes for measurements performed (a, b) in argon and (c, d) under fixed P(I_2). The resistance data are normalized by the total overlap W in the device (see Figure 2b in main text). A significant intercept is found from fitting a line to the R_{eon} vs L data, indicating an interfacial resistance in the order of $R^{\perp}_{eon}$~65

GΩ cm. Such value is fractionally smaller when the $P(I_2)$ is increased, as shown in (e), where the ratio between the intercept $R_{eon}(L = 0)$ and the resistance data is displayed for different values of L. The trend could be consistent with the presence of an inversion layer at the MAPI/Al_2O_3 interface where n-type conduction is significant at low $P(I_2)$ (see Ref. 52 in the main text), and a hole accumulation (electron depletion) layer close to the MAPI/Au interface. The latter introduces a significant interfacial resistance for electrons and its contribution is larger at low $P(I_2)$, as shown in (e). A similar analysis for the ionic interfacial resistance shows relatively low values of the intercept $R_{ion}(L = 0)$. When normalized by the values of ionic resistance, the analysis yields a less clear trend suggesting overall less significant role of the interfacial contribution. This is consistent with the depletion of iodide vacancies in proximity of the MAPI/Al_2O_3 interface.

4. Impedance fitting results

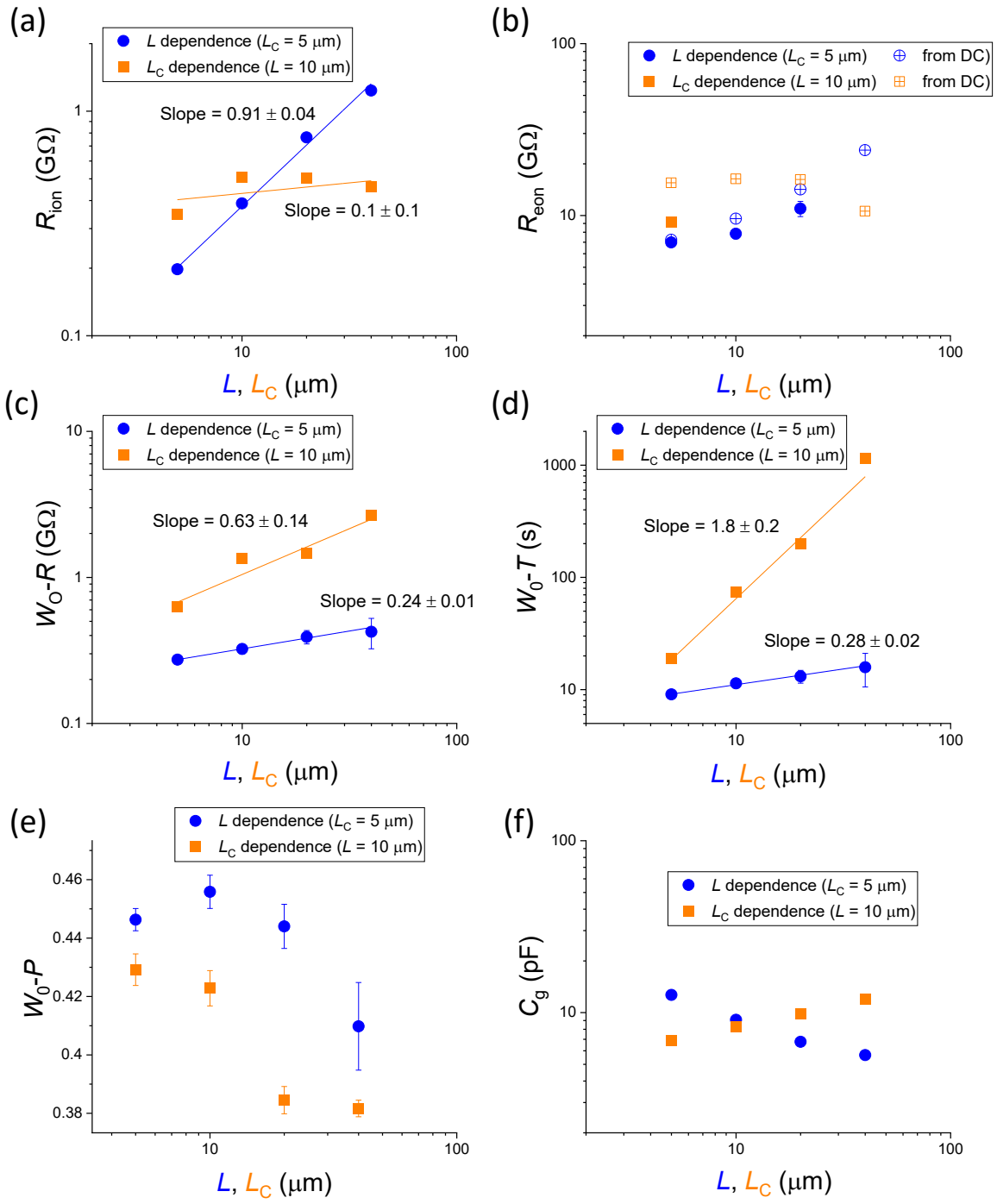

Figure S6. (a–f) Value of the fitting parameters of the elements in the equivalent circuit model shown in Figure 6a in the main text. Note that the parameter R_{eon} used in the main text was extracted from the long time scale DC polarization (Figure 4 in main text). Its value extracted from the fit is reported in (b) only for the cases where it significantly influenced the fit to the data. The fitted values of R_{eon} agree with the ones from DC within a factor of <2. For the other cases (data points not shown), R_{eon} did not influence the final fit significantly, with the fitting result giving very large error for its value.

5. Equivalent circuit model considering ionic disorder at equilibrium

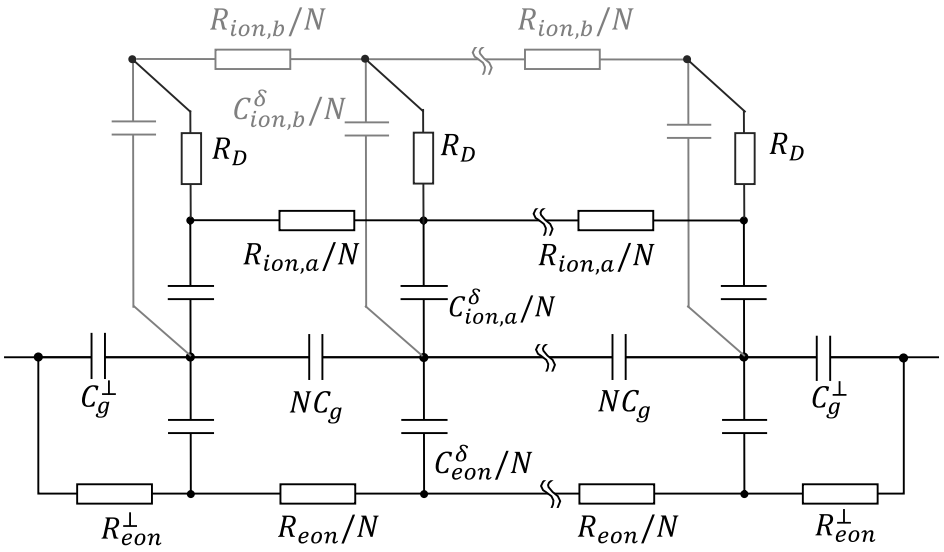

Figure S7. Equivalent circuit model including an ionic disorder resistor that accounts for the local equilibration of two mobile ionic defects following a specific disorder reaction. E.g., for Schottky disorder, according to $\mathrm{M}^{\times}_{\mathrm{MA}} + \mathrm{I}^{\times}_{\mathrm{I}} \rightleftharpoons \mathrm{V}'_{\mathrm{MA}} + \mathrm{V}^{\cdot}_{\mathrm{I}} + \mathrm{MAI}$, a perturbation in the $\tilde{\mu}_{\mathrm{V}^{\cdot}_{\mathrm{I}}}$ causes a local response in $\tilde{\mu}_{\mathrm{V}'_{\mathrm{MA}}}$ based on R_D which represents the kinetics of the disorder equilibrium reaction. For very small values of R_D, the two ionic rails can be condensed to a single ionic rail with effective transport and storage parameters ($R_{ion} = \frac{R_{ion,a}R_{ion,b}}{R_{ion,a}+R_{ion,b}}$ and $C^{\delta}_{ion} = C^{\delta}_{ion,a} + C^{\delta}_{ion,b}$).

6. Numerical solutions and analytical approximations to the transmission line problem

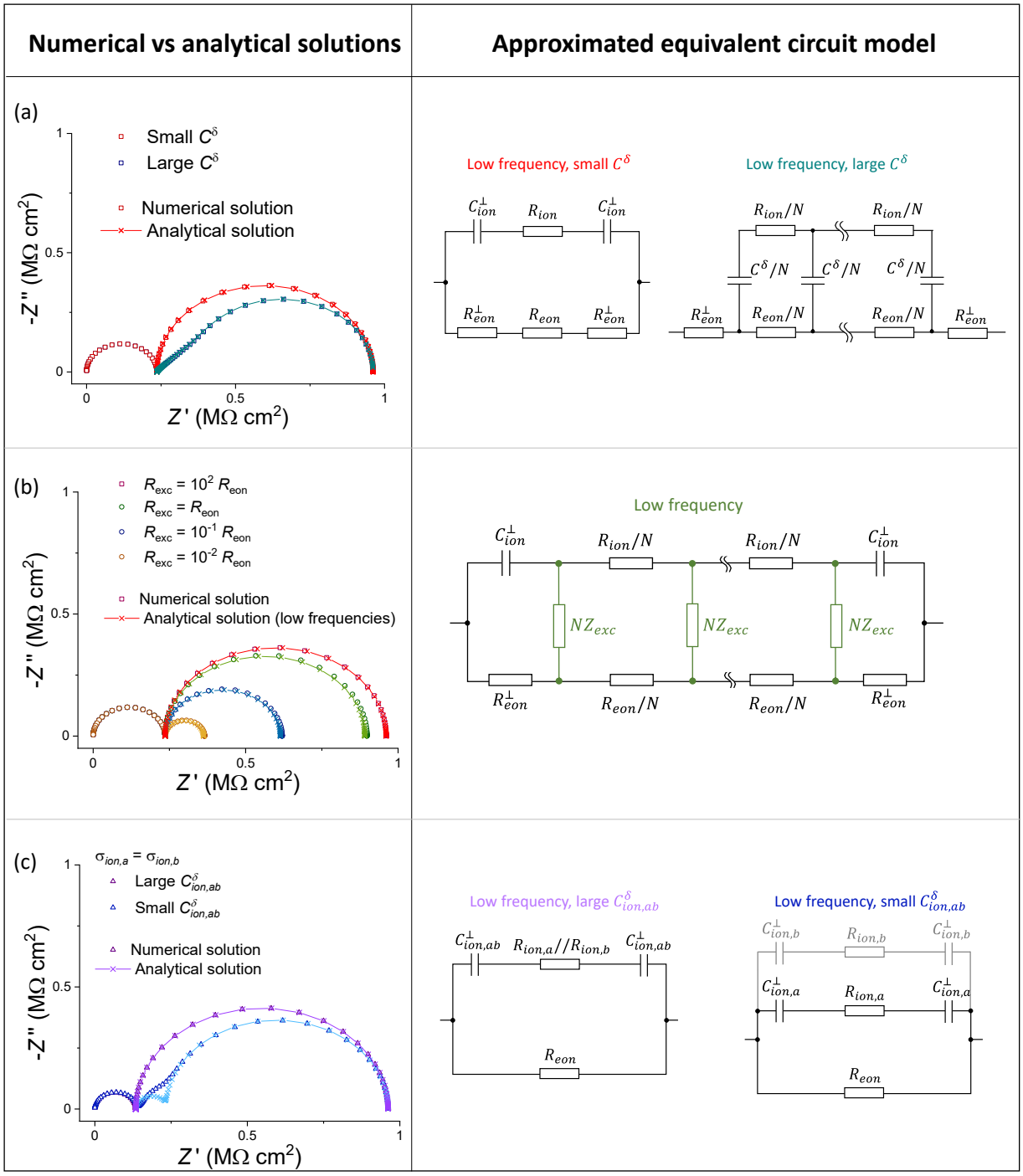

Figure S8. Numerical solution to the transmission line model compared with the analytical solution calculated from the approximated equivalent circuit models associated with the low frequency behavior of a mixed conductor with different properties: (a) chemical capacitance between ionic and electronic defects; (b) exchange of a component (e.g. iodine) with the gas phase; (c) chemical capacitance associated with two ionic species. Frequency range $10^{-5} - 10^{4}$ Hz, 10 points per decade.

We list the analytical expressions for the impedance associated with the approximated equivalent circuit models in Figure S8. The impedance for (a) and (b) in Figure S8 can be expressed based on previous work (J. Jamnik and J. Maier, J. Electrochem. Soc., 146, 4183 (1999), W. Lai and S. M. Haile, J. Am. Ceram. Soc., 88, 2979–2997 (2005)) as:

(a) Small C^{δ}

$$Z = (2R_{eon}^{\perp} + R_{eon}) \frac{1+\frac{i\omega R_{ion} C_{ion}^{\perp}}{2}}{1+\frac{i\omega (R_{ion}+2R_{eon}^{\perp}+R_{eon}) C_{ion}^{\perp}}{2}} \quad \text{Eq. S1}$$

(a) Large C^{δ}

$$Z = 2kR_{eon}^{\perp} + \frac{R_{ion}R_{eon}}{R_{eon}+R_{ion}} + \frac{2R_{eon}^{2}\tanh\left[\frac{k}{2}\right]}{k(R_{eon}+R_{ion})} \quad \text{Eq. S2}$$

where $= \sqrt{i\omega(R_{ion}+R_{eon})C^{\delta}}$.

(b) Component exchange

$$Z = \frac{kR_{ion}R_{eon}+2kR_{eon}^{\perp}(R_{eon}+R_{ion})+2R_{eon}^{2}\tanh\left[\frac{k}{2}\right]}{k(R_{eon}+R_{ion})} \times \frac{1+\frac{i\omega C_{ion}^{\perp}}{2}\frac{R_{eon}R_{ion}\left[kR_{eon}^{\perp}+(R_{ion}+R_{eon})\tanh\left[\frac{k}{2}\right]\right]+2R_{ion}^{2}R_{eon}^{\perp}\tanh\left[\frac{k}{2}\right]}{\frac{k}{2}R_{eon}R_{ion}+kR_{eon}^{\perp}(R_{ion}+R_{eon})+R_{eon}^{2}\tanh[k/2]}}{1+\frac{i\omega C_{ion}^{\perp}}{2}\left[2R_{eon}^{\perp}+2(R_{ion}+R_{eon})\frac{\tanh\left[\frac{k}{2}\right]}{k}\right]}$$

Eq. S3

where $= \sqrt{\frac{R_{ion}+R_{eon}}{Z_{exc}}}$.

Assuming $R_{eon}^{\perp} = 0$, the expression is simplified:

$$Z = \frac{R_{eon}\left(kR_{ion}+2R_{eon}\tanh\left[\frac{k}{2}\right]\right)}{k(R_{eon}+R_{ion})} \times \frac{1+\frac{i\omega C_{ion}^{\perp}}{2}R_{ion}\left[(R_{ion}+R_{eon})\tanh\left[\frac{k}{2}\right]\right]}{1+\frac{i\omega C_{ion}^{\perp}}{2}(R_{ion}+R_{eon})2\frac{\tanh\left[\frac{k}{2}\right]}{k}} \quad \text{Eq. S4}$$

For negligible exchange with the gas phase ($Z_{exc} \to \infty$), Eq. S4 becomes:

$$Z = R_{eon}\frac{1+\frac{i\omega C_{ion}^{\perp}}{2}R_{ion}}{1+\frac{i\omega C_{ion}^{\perp}}{2}(R_{ion}+R_{eon})} \quad \text{Eq. S5}$$

as expected for the equivalent circuit shown in Figure 3b in the main text.

For very fast exchange ($Z_{exc} \to 0$), the impedance becomes purely resistive:

$$Z = \frac{R_{ion}R_{eon}}{R_{ion}+R_{eon}} \quad \text{Eq. S6}$$

(c) 2 ions, large $C_{ion,ab}^{\delta}$

$$Z = R_{eon}\frac{1+\frac{i\omega R_{ion,tot} C_{ion,ab}^{\perp}}{2}}{1+\frac{i\omega (R_{ion,tot}+R_{eon}) C_{ion,ab}^{\perp}}{2}} \quad \text{Eq. S7}$$

Where $R_{ion,tot} = R_{ion,a}R_{ion,b}/(R_{ion,a}+R_{ion,b})$

(c) 2 ions, small $C^{\delta}_{ion,ab}$

$Z = R_{eon}Z_{ion}/(R_{eon} + Z_{ion})$ Eq. S8

where $Z_{ion} = Z_{ion,a}Z_{ion,b}/(Z_{ion,a} + Z_{ion,b})$

given $Z_{ion,a} = \frac{\left(1+\frac{i\omega R_{ion,a}C^{\perp}_{ion,a}}{2}\right)}{\frac{i\omega R_{ion,a}C^{\perp}_{ion,a}}{2}}$ and $Z_{ion,b} = \frac{\left(1+\frac{i\omega R_{ion,b}C^{\perp}_{ion,b}}{2}\right)}{\frac{i\omega R_{ion,b}C^{\perp}_{ion,b}}{2}}$

Note that the analytical solution for this last condition poorly matches the numerical solution at intermediate frequencies. This is because, even considering a four order of magnitude smaller concentration and four order of magnitude larger mobility for defect ion, b compared with ion, a, the value of the chemical capacitance associated with the storage of the two ionic species is as high as $C^{\delta}_{ion,ab}{\sim}10^{-5}\ F\ cm^{-2}$. This is smaller but comparable with the space charge capacitance $C^{\perp}_{ion,ab} = 2.6 \times 10^{-5}\ F\ cm^{-2}$. As a result, the two features are slightly merged together in the numerical solution.

7. Iodine partial pressure dependent conductivity data

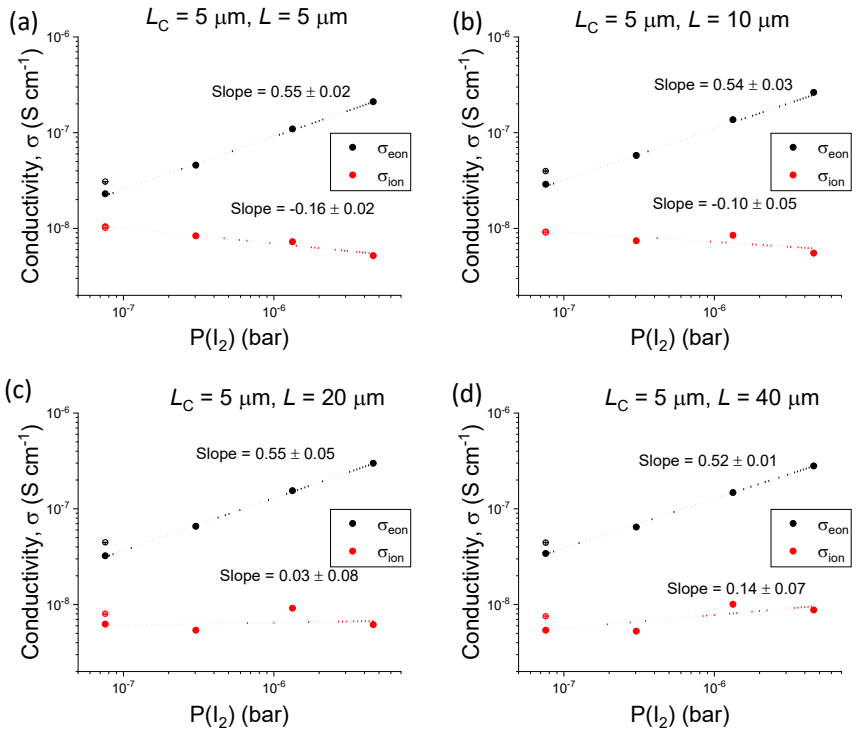

Figure S9. Iodine partial pressure dependence of the electronic and ionic conductivities of MAPI based devices with horizontal architecture (see Figure 3a, b in main text). Data for devices with variable *L* are shown.

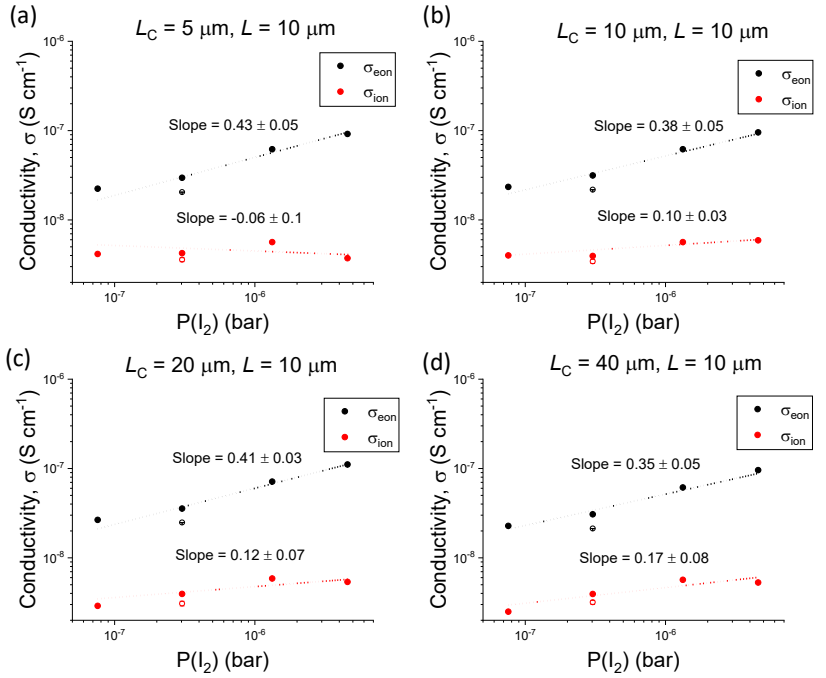

Figure S10. Iodine partial pressure dependence of the electronic and ionic conductivities of MAPI based devices with horizontal architecture (see Figure 3a, b in main text). Data for devices with variable L_C are shown.

8. Analysis of impedance including the effect of grain boundaries

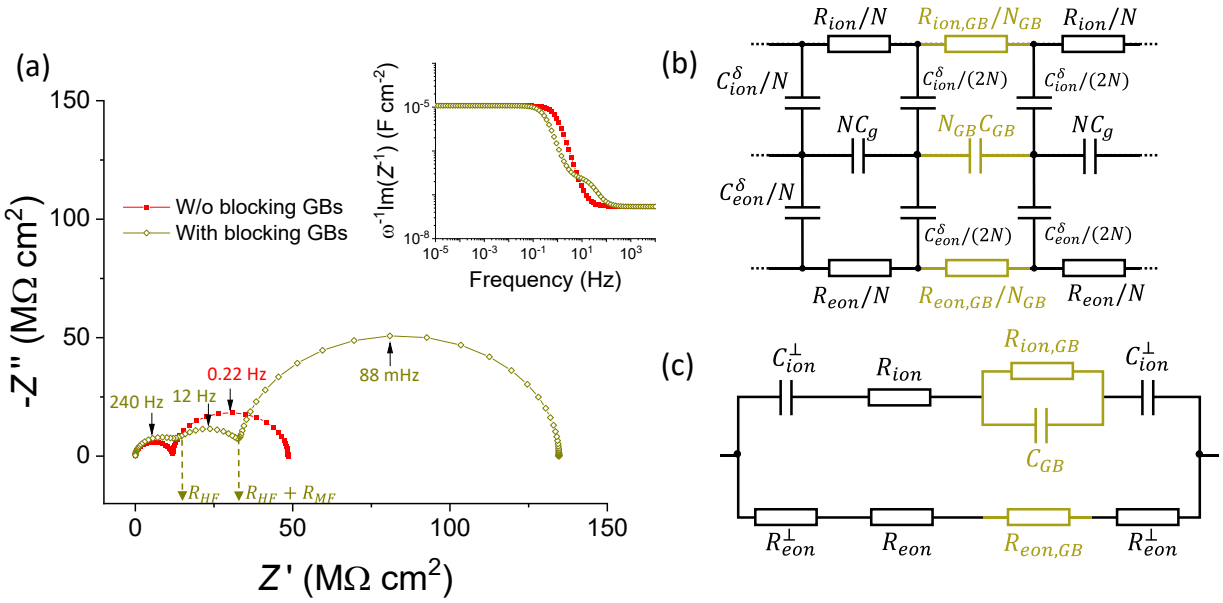

Figure S11. (a) Calculation of impedance using a modified transmission line model where the contribution of grain boundaries is included. The grain boundary resistance for ionic and electronic charge carriers is chosen to have either a negligible or perceptible contribution compared to the corresponding resistance in the grain. The capacitance for each grain boundary was set to $N_{GB}C_{GB} = 10\ \mu F\ cm^{-2}$. For the calculation, a thinner device ($L = 500\ nm$) was considered with a total number of nodes $N = 1000$ to guarantee that the spacing is well below the Debye length in the system (no finer spacing used at interfaces or grain boundaries in this case). (b) Circuit model used for the calculation. The results in (a) show that, for significant grain boundary resistance, an additional feature at intermediate frequencies appears. This can be explained in terms of equivalent circuit model by considering an $R_{ion,GB}C_{GB}$ (in this case input values of $R_{ion,GB} = 2R_{ion}$ and $R_{eon,GB} = 2R_{eon}$ were used) element in the ionic rail (see (c)). Because of the low chemical capacitance of electronic charges considered in this example, the grain boundary resistance $R_{eon,GB}$ is already active at very high frequencies. It follows that, in order to calculate the value of $\sigma_{tot} = \sigma_{ion,tot} + \sigma_{eon,tot}$, one needs to consider $\sigma_{ion,tot} \propto 1/(R_{ion} + R_{ion,GB})$, $\sigma_{eon,tot} \propto 1/(R_{eon} + R_{eon,GB})$). This means that the resistance associated with the total conductivity involves the high frequency feature (R_{HF}) but also the intermediate frequency feature (R_{MF}). Indeed, for the example in (a):

$R_{HF} = (R_{eon} + R_{eon,GB})R_{ion}/(R_{eon} + R_{eon,GB} + R_{ion})$,

$R_{HF} + R_{MF} = (R_{eon} + R_{eon,GB})(R_{ion} + R_{ion,GB})/(R_{eon} + R_{eon,GB} + R_{ion} + R_{ion,GB})$

$= R_{eon,tot}R_{ion,tot}/(R_{eon,tot} + R_{ion,tot})$

Notably, this situation requires a different approach from the one discussed in the main text, where only the high frequency feature is relevant to σ_{tot}, and the mid-frequency feature is related to the device geometry.

9. SEM characterization

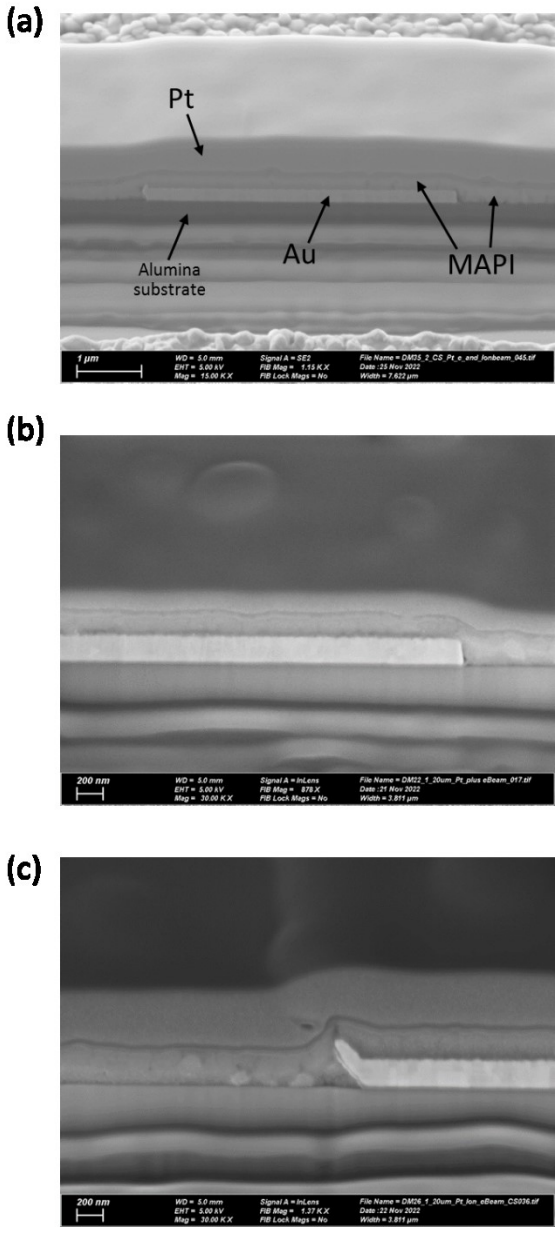

Figure S12. Cross-sectional SEM measurements performed on MAPI films deposited on alumina substrates with interdigitated gold contacts (a ≈ 20 nm thin chromium adhesion layer is used below the gold). Before the FIB (focused ion beam) cutting of the samples, a platinum layer was deposited on the samples, as shown in (a). (b) Image taken close to the edge of the gold contact. The image shows that MAPI covers the metal and it has similar thickness on top of the gold and on the alumina substrate. (c) Example of a sample where the edge of the gold contact is slightly lifted due to the lift-off process used to fabricate the interdigitated metal electrodes. Even in this case, MAPI covers the surface of the metal and is in contact with the active area of the device.

10.X-ray diffraction characterization

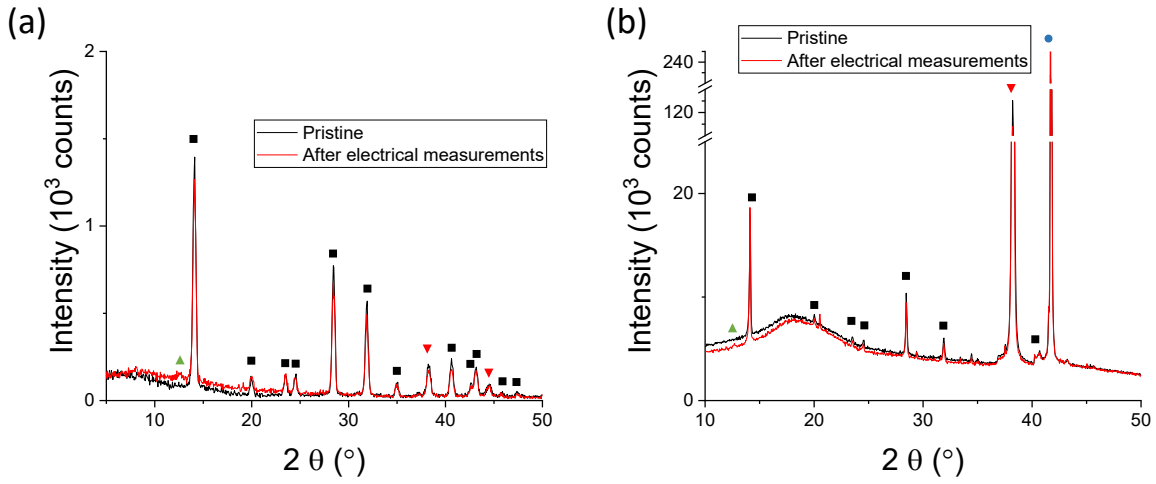

Figure S13. X-ray diffraction characterization of MAPI based devices with horizontal architecture before and after the electrical characterization. Data acquired using (a) Grazing-incidence and (b) Bragg-Brentano geometry. All measurements were performed with the sample in a gas-tight dome under argon. Symbols indicate the peaks for: (black squares) tetragonal MAPI; (green upward pointing triangles) PbI_2; (blue circles) alumina; (red downward pointing triangles) gold.

11. Input parameters for impedance calculations

Table S1. List of reference values used for the calculation of impedance in the main text (red data set in Figure 3 and 7). All electrical parameters are normalized by the active area of the device.

Parameter	Value
R_{eon}	0.96 MΩ cm^2
R_{ion}	0.31 MΩ cm^2
C_{eon}^{δ}	4 pF cm^{-2}
C_{ion}^{δ}	123 mF cm^{-2}
C_g	2.8 nF cm^{-2}
$C_{g,c}^{\perp}$	1 mF cm^{-2}

Table S2. Material and device parameters used to evaluate some of the equivalent circuit model parameters in Table S1.

Parameter	Value
p	6.5 10^8 cm^{-3}
$[V_I^{\cdot}]$	2 10^{19} cm^{-3}
u_p	10 cm^2 V^{-1} s^{-1}
$u_{V_I^{\cdot}}$	10^{-9} cm^2 V^{-1} s^{-1}
ϵ_r	32
L	10 µm

To obtain the cyan data set in Figure 3 (large C^{δ}), a trapping factor of $\chi_{eon} = 10^{-9}$ was used. In the calculation, this was implemented by considering values of p = 6.5 10^{17} cm^{-3} and u_p = 10^{-8} cm^2 V^{-1} s^{-1}. This choice results in the same value of R_{eon} as in Table S1, while implying a much larger value for the electronic chemical capacitance (C_{eon}^{δ} = 4 mF cm^{-2}). All the other calculated impedance spectra shown in Figure 7 in the main text were obtained by using the parameters in Table S1. Additional parameters related to the second mobile ionic defect and component exchange with the gas phase were included as described in the main text and in the Figure's legend.